

Article

Sea-Cucumber-like Microstructure Polyoxometalate/TiO₂ Nanocomposite Electrode for High-Performance Electrochromic Energy Storage Devices

Xiaoshu Qu , Lili Zhou, Zefeng Liu, Zeyu Wang, Jilong Wang, Xiaoyang Yu, Hua Jin and Yanyan Yang *

College of Chemical and Pharmaceutical Engineering, Jilin Institute of Chemical Technology, Jilin 132022, China
* Correspondence: xiaoshuqu@jlicet.edu.cn (X.Q.); yyy200409@163.com (Y.Y.)

Abstract: The key challenge in the practical application of electrochromic energy storage devices (EESDs) is the fabrication of high-performance electrode materials. Herein, we deposited K₇[La(H₂O)_x(α₂-P₂W₁₇O₆₁)] (P₂W₁₇La) onto TiO₂ nanowires (NW) to construct an NW-P₂W₁₇La nanocomposite using a layer-by-layer self-assembly method. In contrast to the pure P₂W₁₇La films, the nanocomposite exhibits enhanced electrochromic and electrochemical performance owing to the 3D sea-cucumber-like microstructure. An EESD using the NW-P₂W₁₇La film as the cathode exhibited outstanding electrochromic and energy storage properties, with high optical modulation (48.6% at 605 nm), high switching speeds (t_{coloring} = 15 s, t_{bleaching} = 4 s), and high area capacitance (5.72 mF cm⁻² at 0.15 mA cm⁻²). The device can reversibly switch between transparent and dark blue during the charge/discharge process, indicating that electrochromic contrast can be used as a quantitative indicator of the energy storage status.

Keywords: electrochromism; energy storage; polyoxometalate; nanostructures; EESD



Citation: Qu, X.; Zhou, L.; Liu, Z.; Wang, Z.; Wang, J.; Yu, X.; Jin, H.; Yang, Y. Sea-Cucumber-like Microstructure Polyoxometalate/TiO₂ Nanocomposite Electrode for High-Performance Electrochromic Energy Storage Devices. *Molecules* **2023**, *28*, 2634. <https://doi.org/10.3390/molecules28062634>

Academic Editors: Konstantin Brylev and Yann Molard

Received: 21 February 2023

Revised: 7 March 2023

Accepted: 7 March 2023

Published: 14 March 2023



Copyright: © 2023 by the authors. Licensee MDPI, Basel, Switzerland. This article is an open access article distributed under the terms and conditions of the Creative Commons Attribution (CC BY) license (<https://creativecommons.org/licenses/by/4.0/>).

1. Introduction

Amidst increasing environmental pollution and the gradual exhaustion of non-renewable energy resources, the development of controllable devices for energy storage, conversion, and protection, such as smart windows [1–3], micro-supercapacitors [4,5], lithium-ion batteries [6,7], electrochemical capacitors [8,9], and solar cells [10,11], has become a global priority. Electrochromic (EC) devices and batteries/pseudocapacitors have similar electrode materials, device structures, and faradaic reactions [12]. Integrating electrochromic and energy storage properties into a single platform to construct electrochromic energy storage devices (EESDs) enables versatile use of energy and significantly reduces the cost of energy storage [13–16]. EESDs change color in real time based on the level of stored energy and have the potential to be used in new smart electronic products [17], smart clothing [18], and military equipment [19].

A challenge in the development of EESDs is the fabrication of high-performance electrode materials. Recently, bifunctional electrode materials, such as WO₃ [20], V₂O₅ [21], NiO [22], and Prussian white [23], have attracted significant attention. Deng et al. [24] fabricated MnO₂/WO₃ EC electrodes with ultra-long stability and excellent optical modulation, and assembled all-solid-state zinc-ion supercapacitors with high coloration efficiency and cycling stability. Zhang et al. [25] constructed asymmetric electrochromic supercapacitors based on a new conjugated polymer (PETC) and V₂O₅ ion-storage material, which outperformed other conjugated polymer-based electrochromic supercapacitors in terms of electrochemical performance. Polyoxometalates (POMs) are ideal EC and electrochemical storage materials. Owing to their unique multi-electron storage capacity and rich redox properties, POMs have been extensively studied for use in EC and energy-related technologies [26–29]. Fan et al. [30] prepared a self-supporting composite based on H₃PMo₁₂O₄₀ heterogeneous blue-modified reduced graphite oxide (PAHB/RGO), which had a specific

capacitance of 395 F g^{-1} at 1 A g^{-1} . The symmetrical solid-state supercapacitor assembled with PAHB/RGO electrodes had excellent specific energy and power. Zhang et al. [31] prepared flexible amorphous isopolytungstate electrochromic devices using inkjet printing technology and observed quantitative color changes in response to different voltages.

There is currently a dearth of research on POM-based EESDs. Recently, our research group investigated several high-performance electrochromic energy storage bifunctional composites containing saturated [32], lacunary [33], and substituted-type [34] POMs. In this study, we further developed a POM-based EESD and studied its EC and energy storage performance. We deposited $\text{K}_7[\text{La}(\text{H}_2\text{O})_x(\alpha_2\text{-P}_2\text{W}_{17}\text{O}_{61})]$ (abbreviated as $\text{P}_2\text{W}_{17}\text{La}$) nanoparticles onto TiO_2 nanowires (TiO_2 NW) to obtain an electrochromic energy storage bifunctional nanocomposite ($\text{NW-P}_2\text{W}_{17}\text{La}$) via a combined hydrothermal and layer-by-layer (LbL) self-assembly method. The 3D sea-cucumber-like microstructure of $\text{NW-P}_2\text{W}_{17}\text{La}$ enhanced the coverage of the surface, exposed more reactive sites, and shortened the electron/ion diffusion pathways, resulting in rapid reaction kinetics and enhanced electrochemical performance. The optical and electrochemical properties of the $\text{NW-P}_2\text{W}_{17}\text{La}$ nanocomposite were investigated and compared to those of a densely packed structure. An asymmetric EESD was fabricated using an $\text{NW-P}_2\text{W}_{17}\text{La}$ film as the cathode and a TiO_2 nanowire film as the anode.

2. Results and Discussion

2.1. Characterizations of Nanocomposites

Figure 1 depicts the fabrication process of the $\text{NW-P}_2\text{W}_{17}\text{La}$ nanocomposite film. UV/Vis spectroscopy was used to track the growth of the composite film. The deposition of each layer of $\text{P}_2\text{W}_{17}\text{La}$ was accompanied by a linear increase in absorbance, confirming that the growth of the multilayer film obtained via electrostatic self-assembly was uniform and orderly, and that the convenient LbL method can achieve controlled thin-film growth (Figure S1).

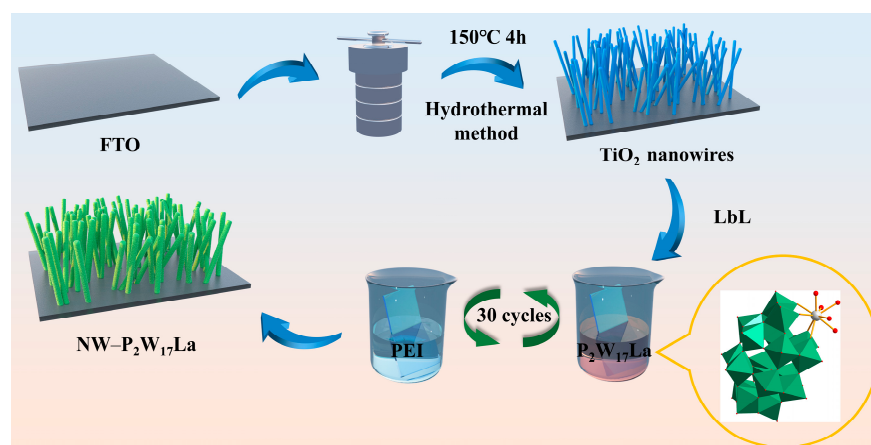


Figure 1. Fabrication process of the $\text{NW-P}_2\text{W}_{17}\text{La}$ nanocomposite film.

For comparison, a pure POM film was fabricated on a fluorine-doped tin oxide (FTO) substrate using the same method (denoted as $\text{FTO-P}_2\text{W}_{17}\text{La}$). Scanning electron microscopy (SEM) images of the $\text{FTO-P}_2\text{W}_{17}\text{La}$ film and $\text{NW-P}_2\text{W}_{17}\text{La}$ film are shown in Figure 2a,b. The $\text{FTO-P}_2\text{W}_{17}\text{La}$ film exhibits a tightly packed microstructure; the FTO surface is densely covered with aggregates of $\text{P}_2\text{W}_{17}\text{La}$ and polyetherimide (PEI), forming a cobblestone-like morphology. Figure S2 shows the vertically grown TiO_2 nanowires obtained via hydrothermal synthesis. Compared with the pure TiO_2 NW film, the nanowires in the $\text{NW-P}_2\text{W}_{17}\text{La}$ film are thicker and denser because of the encapsulation of $\text{P}_2\text{W}_{17}\text{La}$ nanoparticles and PEI, forming a 3D sea-cucumber-like microstructure. The TiO_2 nanowires act as a skeleton on which the POM nanoparticles are deposited, thereby avoiding aggregation and exposing more reactive sites. The cross-sectional image shows that the $\text{NW-P}_2\text{W}_{17}\text{La}$ composite film

can reach a thickness of 620 nm, whereas the FTO- $P_2W_{17}La$ film is approximately 110 nm thick. This demonstrated that the 3D sea-cucumber-like microstructure of NW- $P_2W_{17}La$ enhanced the coverage of the surface and provided more electron/ion diffusion pathways. Additionally, as shown in Figure S3, W, P, La, and Ti are homogeneously dispersed in the energy-dispersive X-ray spectroscopy (EDS) maps of the NW- $P_2W_{17}La$ composite, confirming that the $P_2W_{17}La$ nanoparticles are uniformly attached to the TiO_2 nanowires.

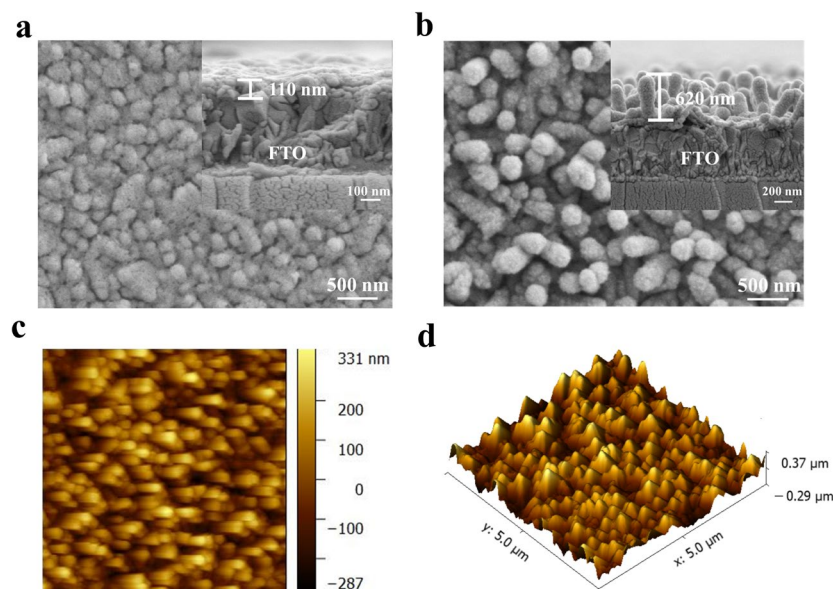


Figure 2. SEM images of (a) FTO- $P_2W_{17}La$ and (b) NW- $P_2W_{17}La$ composite films (insets: cross-sectional images). (c) Two-dimensional (2D) and (d) 3D AFM images of the NW- $P_2W_{17}La$ composite film.

The surface topographic features and roughness of the films were examined using atomic force microscopy (AFM) (Figures 2c,d and S4). The thicknesses of the NW- $P_2W_{17}La$ composite film and FTO- $P_2W_{17}La$ measured by AFM were 618 nm and 164.1 nm, respectively, which agree well with the features observed in the SEM images. The root-mean-square roughness of the NW- $P_2W_{17}La$ and FTO- $P_2W_{17}La$ films were calculated to be 108.1 nm and 26.4 nm (with an area of $5 \times 5 \mu m^2$), respectively. The 3D sea-cucumber-like microstructure increases the roughness of the material, thereby increasing the active reaction surface area.

The transmission electron micrograph (TEM) of unmodified TiO_2 nanowires scraped from the FTO substrate (Figure 3a) clearly shows the morphology and size of the nanowires. Figure 3b shows the microstructure of the NW- $P_2W_{17}La$ film and the further characterization of the area between the TiO_2 NW and $P_2W_{17}La$ nanoparticles. After the self-assembly step, the surfaces of the nanowires were coated with $P_2W_{17}La$ nanoparticles (Figure 3b). The TEM-EDS element maps of the NW- $P_2W_{17}La$ film are shown in Figures 3c and S5. The TEM images and corresponding EDS maps confirm that W, P, Ti, and La are uniformly distributed, indicating that the $P_2W_{17}La$ particles enclose the TiO_2 nanowires to form a core-shell-like structure.

The chemical composition and element valence states of the NW- $P_2W_{17}La$ film were further studied using high-resolution X-ray photoelectron spectroscopy (XPS) (Figure 3d–f). In the deconvoluted XPS spectrum shown in Figure 3d, the strong doublet peaks at 455.8 eV and 461.7 eV are observed, corresponding to Ti 2p_{3/2} and Ti 2p_{1/2}, respectively, indicating that TiO_2 was successfully constructed on the FTO substrate [35,36]. As shown in Figure 3e, the strong doublet peaks at 35.1 and 37.2 eV are associated with the binding energies of electrons in the W 4f_{7/2} and W 4f_{5/2} orbitals, respectively, indicating that all of the W atoms in the composite film are in the +6 valence state [37]. The W^{VI} atoms can be reduced

591 nm reached 90%. The NW-P₂W₁₇La composite film exhibits a coloring time of 12 s and a bleaching time of 4 s, whereas the FTO-P₂W₁₇La film requires 10 s and 2 s, respectively. Coloration efficiency (CE) measures the correlation between the optical change and the charge consumption [40]. Figure 4c illustrates the variation in the optical density versus the charge density from the electrolyte to the film. The CE value of the NW-P₂W₁₇La film (91.7 cm² C⁻¹) is higher than that of the FTO-P₂W₁₇La film (46.6 cm² C⁻¹), indicating that a large transmittance modulation can be achieved with a small charge input. The electrochemical cyclic stability of the NW-P₂W₁₇La film was evaluated over 1000 cycles of double-potential steps at 591 nm. The NW-P₂W₁₇La film retained an optical contrast of approximately 96.9% of its initial value (Figure 4d), whereas the FTO-P₂W₁₇La film retained approximately 82.9% of its initial value (Figure S6). As shown in Figures S7 and S8, the morphology of NW-P₂W₁₇La did not change noticeably after 1000 cycles. The experimental results show that the sea-cucumber-like nanostructure conferred improved EC properties compared with the densely packed FTO-P₂W₁₇La structure.

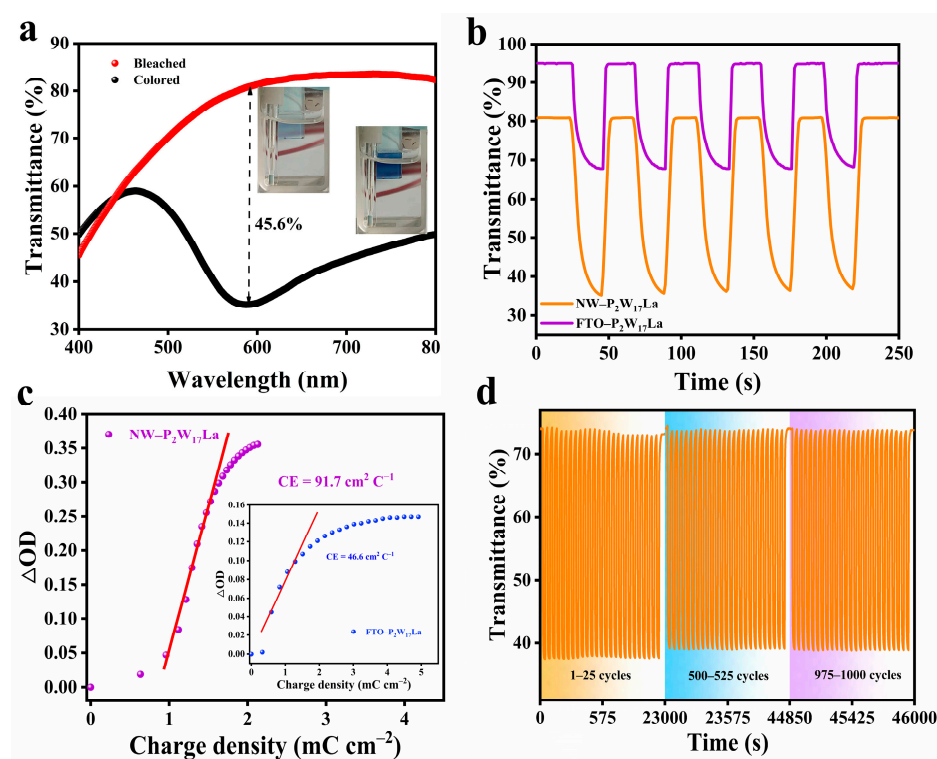


Figure 4. (a) Visible transmittance spectra of the NW-P₂W₁₇La composite film in the bleached and colored states at 0 V and -1.3 V (insets: digital photographs). (b) In situ transmittance curves of the FTO-P₂W₁₇La and NW-P₂W₁₇La films at 591 nm during pulse voltages (-1 V and +1 V). (c) Plot of optical contrast versus charge density for NW-P₂W₁₇La and FTO-P₂W₁₇La films. (d) Cycle stability of NW-P₂W₁₇La film at 591 nm under pulse voltages of -1 V and +1 V.

2.3. Capacitive Performance of Electrodes

The electrochemical properties of as-prepared films were measured using cyclic voltammetry (CV) and galvanostatic charge/discharge (GCD) tests. The three pairs of redox peaks on the NW-P₂W₁₇La film CV curve are attributed to the redox reaction between W^{VI} and W^V and represent typical faradaic behavior during ion insertion/extraction (Figure 5a) [41]. When the scan rate is increased from 10 to 100 mV s⁻¹, the shapes of the curves remain largely unchanged, except that the peak potential exhibits a minor shift. The anodic peaks shift toward positive potentials and cathodic peaks shift toward negative potentials, which can be attributed to a reversible but nonideal redox process [42]. To reveal the electrochemical kinetic process, the relationship between the oxidation/reduction peak

current and the scan rate was studied. The peak current density i and the corresponding scan rate v follow the mathematical relationship $i = av^b$, where a is an adjustable parameter and b is the slope of the linear $\log i$ versus $\log v$ curve. The magnitude of the slope can be used to characterize the ion storage mechanism during charging and discharging [43]. When $b = 0.5$, the electrochemical reaction process is governed by the diffusion-controlled process, whereas $b = 1$ indicates that the process is primarily controlled by the surface reaction, resulting in a capacitance-controlled process. The linear relationship between $\log i$ and $\log v$ is shown in Figure 5b and the b -values of peaks I and II are 0.68 and 0.60, respectively. This shows that the kinetic process taking place in the NW-P₂W₁₇La film is controlled by ion diffusion and capacitive effects.

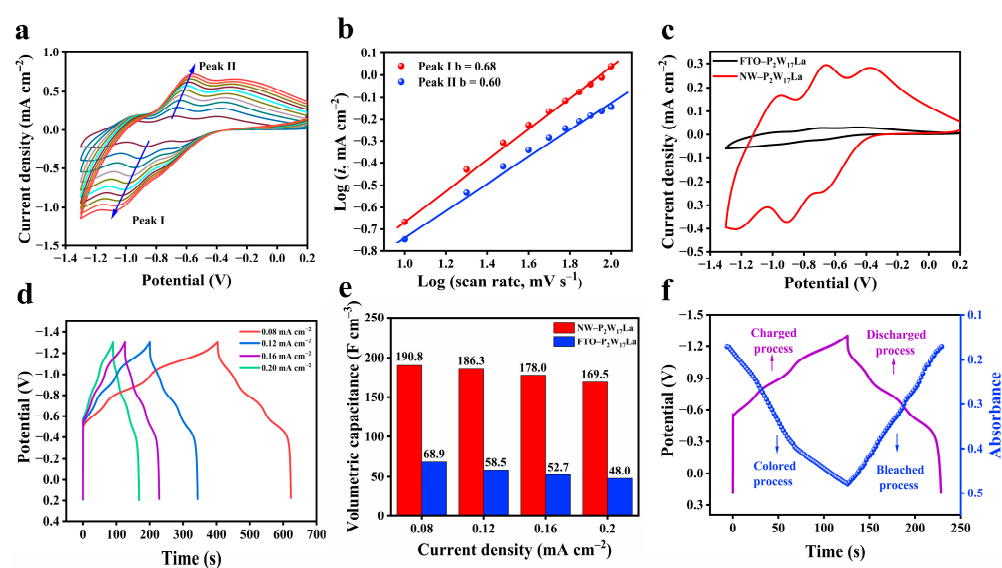


Figure 5. (a) CV curves of the NW-P₂W₁₇La film at different scan rates (10–100 mV/s) within the range of −1.3 V to +0.2 V. (b) Logarithmic relationship between the oxidation/reduction peak current density (i) and scan rate. (c) CV curves for NW-P₂W₁₇La and FTO-P₂W₁₇La films with 20 mV/s. (d) GCD profiles of the NW-P₂W₁₇La film at different current densities. (e) Comparison of the volumetric capacitances of FTO-P₂W₁₇La and NW-P₂W₁₇La films under various current densities. (f) In situ absorbance evolution at 591 nm during the charge/discharge process of the NW-P₂W₁₇La film in the voltage range of −1.3 V to +0.2 V.

Figures S9 and 5c show CV curves of the NW-P₂W₁₇La, FTO-P₂W₁₇La, and TiO₂ NW films obtained at the same scan rate in 1 Mol L^{−1} LiClO₄/propylene carbonate (PC). The NW-P₂W₁₇La film shows the largest peak current value, demonstrating its high conductivity and low internal resistance characteristics. According to the results presented in Figure 5c, at the scan rate of 20 mV s^{−1}, the surface coverage of NW-P₂W₁₇La was determined to be 1.74×10^{-6} mol cm^{−2}, which is higher than that of the tightly packed FTO-P₂W₁₇La film (3.61×10^{-7} mol cm^{−2}) [44]. Diffusion coefficients (D) of Li⁺ ions were calculated using the Randles–Sevick equation [45]. The D value obtained for the NW-P₂W₁₇La film is 1.28×10^{-12} cm s^{−1}, and that computed for the FTO-P₂W₁₇La film is 1.10×10^{-14} cm s^{−1}. The higher Li-ion diffusion rate obtained for NW-P₂W₁₇La confirms the excellent electrical conductivity of this material.

The GCD measurements of the NW-P₂W₁₇La film are shown in Figure 5d. The shapes of the GCD profiles under different current densities were similar, showing the superior charge/discharge reversibility of the material. Notably, there are three plateaus in the GCD curves and their positions are consistent with those in the CV curves, indicating sound pseudocapacitive behavior. Figure 5e illustrates the volumetric capacitances as a function of the current densities for the FTO-P₂W₁₇La and NW-P₂W₁₇La films. The volumetric capacitance of both films gradually decreases with the increasing current density,

which may be due to insufficient ion diffusion during the charge/discharge process at higher current densities. The NW-P₂W₁₇La film achieves a high volumetric capacitance of 190.8 F cm⁻³ at 0.08 mA cm⁻², whereas that of the FTO-P₂W₁₇La film is significantly lower, reaching 68.9 F cm⁻³ at 0.08 mA cm⁻². The excellent energy storage performance of the NW-P₂W₁₇La film is primarily due to its 3D sea-cucumber-like microstructure, which is conducive to rapid reaction kinetics.

Figure 5f shows the GCD curve of the NW-P₂W₁₇La film at 0.16 mA cm⁻², overlaid with the in situ absorbance curve at 591 nm. During the charging process, the NW-P₂W₁₇La film exhibits a noticeable increase in absorbance, whereas during discharging, the absorbance reversibly decreases. There is a clear relationship between absorbance and charge storage; therefore, the storage state of charge can be quantitatively monitored using the absorbance value.

For comparison, some recently reported EC energy storage materials based on POMs and inorganic metal oxides are listed in Table S1, and our current system exhibits comparable or superior performance. In addition, the transmittance modulation and coloration efficiency of the lacunary and substituted Dawson structures are higher than that of the saturated structure, indicating that the structure and composition of POMs strongly influence their optoelectric properties [46]; therefore, multifunctional properties can be easily adjusted by changing the POM type. In future works, our group will explore the fluorescence regulation ability of the NW-P₂W₁₇La film and POMs with similar structures containing other lanthanides, and develop multifunctional materials based on POMs with multi-band regulation in the visible and fluorescence regions.

2.4. Configuration and Performance of EESD

The schematic diagram in Figure 6a shows the configuration of an NW-P₂W₁₇La film electrode-based electrochromic energy storage device. The asymmetric EESD was assembled using an NW-P₂W₁₇La film as the cathode, a TiO₂ NW film as the anode, and 0.5 M LiI/PC as the electrolyte. TiO₂ has a high transparency and exhibits only an imperceptible light blue color in the reduced state. In addition, it is widely used in EC and lithium-ion batteries [47] because of its fast insertion/extraction and good stability; therefore, the TiO₂ NW film was chosen as the anode of the device. Figure 6b shows digital photographs of the EESD under different voltages. The color of the device undergoes a considerable change from transparent to dark blue, which confirms that the EESD exhibits excellent EC properties and can be applied to visualize and quantify the energy storage state. The optical contrast of the EESD reaches 48.6% at 605 nm (Figure 6c), which complies with the requirement for practical applications. To determine the energy state of the device, the change in light transmittance of the EESD was recorded at different voltages. As shown in Figure S10, as the applied potential increases, the EESD gradually changes from transparent to dark blue, and the transmittance value exhibits a clear correspondence to the applied voltage. This shows that the energy storage level of the device can be visualized and quantified. In addition, high switching speeds of 15 s and 4 s are achieved for the coloring and bleaching processes of the EESD, respectively (Figure 6d), and the CE reaches 47.6 cm² C⁻¹ (Figure 6e). The cyclic charge/discharge curve exhibits a maximum areal capacitance of 5.72 mF cm⁻² at 0.15 mA cm⁻² (Figure 6f,g). Furthermore, the coloring/bleaching process of the EESD is highly synchronized with the charge/discharge process (Figure 6h). Figure 6i shows an LED powered by the EESD. The good performance of the EESD is attributed to the high-performance NW-P₂W₁₇La cathode and the good charge balance and storage capability of the TiO₂ NW anode in the device.

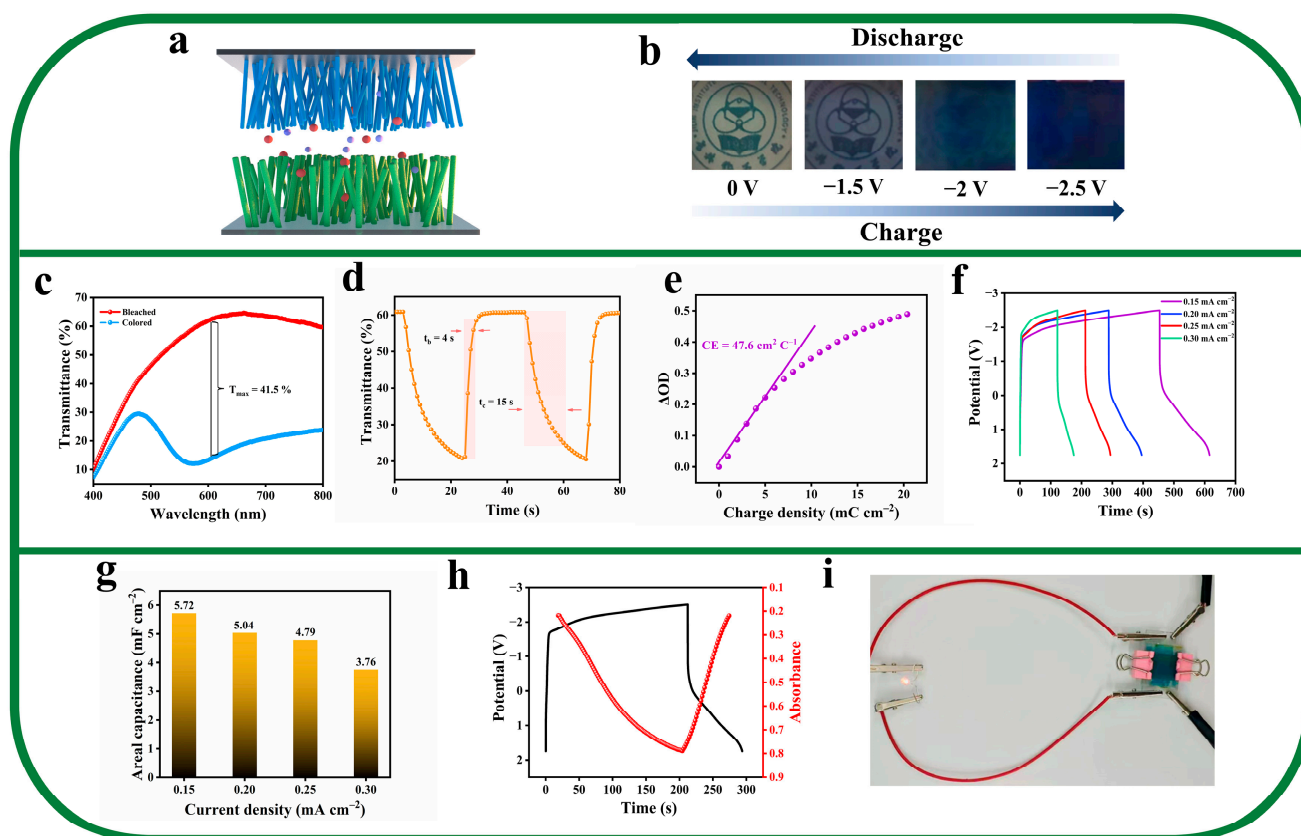


Figure 6. EC and energy storage performance of the EESD. (a) Configuration of the asymmetric EESD containing an NW- $P_2W_{17}La$ film. (b) Digital photographs of color changes of the EESD under different voltages. (c) Transmittance spectra of the EESD in the bleached and colored states at 0 V and -2.5 V in the wavelength range of 400–800 nm. (d) Corresponding in situ transmittance responses for 22 s per step measured at 605 nm. (e) CE of the EESD at 605 nm. (f) EESD constant current charge/discharge curve and (g) Areal capacitance at current densities from 0.15 to 0.3 $mA\ cm^{-2}$. (h) In situ absorbance evolution at 605 nm during the charge/discharge processes of the EESD. (i) Digital photograph of a fully charged bifunctional device powering a red LED.

3. Materials and Methods

3.1. Chemicals

All chemicals were of analytical grade. Fluorine-doped tin oxide (FTO)-coated glass substrates ($<10\ \text{ohm/sq}$) were purchased from Pilkington (Toledo, OH, USA). (3-Aminopropyl) trimethoxysilane (APS) and polyetherimide (PEI) were purchased from Aladdin Bio-Chem Technology Co., Ltd. (Shanghai, China) and used without further treatment. $K_7[La(H_2O)_x(\alpha_2-P_2W_{17}O_{61})]$ ($P_2W_{17}La$) was prepared according to the literature [48–50]. The structure is shown in Figure S11 and characterized using infrared (IR) spectroscopy (Figure S12) and ultraviolet/visible (UV/Vis) absorption spectroscopy (Figure S13).

3.2. Fabrication of Composite Films

The TiO_2 nanowire substrate was synthesized via a hydrothermal synthesis technique according to our previously reported procedure [33]. The multiple-layer film was assembled via the LbL self-assembly method. FTO glass coated with the nanowire substrate was soaked in APS for 12 h, soaked in HCl (pH = 2.0) for 20 min, rinsed with distilled water to remove any HCl attached to the surface, and dried under a nitrogen stream. The nanowire-modified FTO glass was soaked in an aqueous $P_2W_{17}La$ solution ($5 \times 10^{-3}\ \text{mol}\ L^{-1}$) for 7 min, washed with distilled water, and dried under a nitrogen stream. The FTO glass was then immersed in PEI ($5 \times 10^{-3}\ \text{mol}\ L^{-1}$, pH = 4) for 7 min. The POMs and PEI have

opposite charges and are alternately deposited on the substrate via electrostatic attraction. This procedure was repeated 30 times to obtain the NW-P₂W₁₇La film comprising 30 layers of P₂W₁₇La. For comparison, a pure P₂W₁₇La film (denoted as FTO-P₂W₁₇La), which comprised 30 layers of P₂W₁₇La, was fabricated on unmodified FTO glass using the same method.

3.3. Assembly of Asymmetric EESD

An asymmetric bifunctional EESD was assembled using an NW-P₂W₁₇La film as the cathode, a TiO₂ NW film as the anode, and 0.5 M LiI in PC as the liquid electrolyte. First, the two electrodes were sandwiched together with 1 mm double-sided tape. The electrolyte was then injected into the space with a syringe to fabricate the prototype electrochromic energy storage device. The effective area of the device was 1 cm².

3.4. Materials Characterizations

FTIR spectroscopy was conducted using a GangDong FTIR-650 spectrometer (Tianjin, China) between 400 and 4000 cm⁻¹. SEM images were measured on FEI Verios 460 L scanning electron microscope (Hillsboro, OH, USA). AFM images were investigated by Icon Bruker microscope (Ettlingen, Germany). TEM images were measured on a FEI Tecnai G2F20 S-TWIN microscope equipped with an energy-dispersive spectrometer (EDS) (Hillsboro, OH, USA). The TEM sample was prepared by scraping a small amount of the film (0.005 mg) off the FTO substrate and dispersing the powder in 1 mL of an ethanol solution by ultrasonication for 40 min. XPS analysis was measured on a Thermo ESCALAB 250 spectrometer (Shanghai, China).

3.5. Electrochromic and Energy Storage Performance Measurements

The UV/Vis spectra were obtained using a PERSEE TU-1901 spectrometer (Beijing, China). The CV and galvanostatic charge/discharge (GCD) measurements were performed using an CHI660B Chenhua electrochemical workstation (Shanghai, China) in a three-electrode configuration, where the as-prepared film served as the working electrode, Ag/AgCl (3 M KCl) as the counter electrode, Pt wire/Pt plate as the reference electrode, and LiClO₄/PC (1 Mol L⁻¹) as the electrolyte. The electrochromic and capacitive properties were studied using in situ TU-T9S PERSEE UV/Vis spectrometry (Beijing, China) with an CHI660B Chenhua electrochemical workstation (Shanghai, China). The EESD was characterized using a two-electrode system.

4. Conclusions

We synthesized a bifunctional nanocomposite film comprising POMs and TiO₂ nanowires and constructed an EESD by assembling the film with a TiO₂ nanowire-film cathode. Compared with a densely packed structure, the loose 3D sea-cucumber-like microstructure provides a larger active surface area and shortens the electron/ion diffusion pathways, leading to uniform and fast redox reaction kinetics and simultaneously enhancing the EC and electrochemical performance of the composite. The designed EESD exhibits large optical contrast (48.6% at 605 nm), high switching speeds ($t_c = 15$ s, $t_b = 4$ s), and high areal capacitance (5.72 mF cm⁻² at 0.15 mA cm⁻²). The developed device can power an LED bulb and function as a smart energy storage device where the level of stored energy can be visually and quantitatively monitored using rapid and reversible color variation. This work provides a novel paradigm for POM-based EESDs for optical-electrochemical energy applications.

Supplementary Materials: The following supporting information can be downloaded at: <https://www.mdpi.com/article/10.3390/molecules28062634/s1>, Figure S1. UV–vis absorption spectra of NW–P₂W₁₇La film (number of cycles: 0–30). Inset: plots of the absorbance values at 198 and 280 nm. Figure S2. The SEM image of TiO₂ NW. Figure S3. SEM-EDS mapping of NW–P₂W₁₇La for P, W, Ti and La, respectively. Figure S4. The 2D (a) and 3D (b) AFM images of FTO–P₂W₁₇La. Figure S5. TEM-EDS elemental mapping patterns of P. Figure S6. Cycle stability of FTO–P₂W₁₇La film at 591 nm under square wave potentials of –1V and +1V. Figure S7. The AFM of NW–P₂W₁₇La film after cycle stability test. Figure S8. The SEM of NW–P₂W₁₇La film after cycle stability test. Figure S9. CV curve of TiO₂ NW film at a scan rate of 20 mV/s with LiClO₄/PC as the electrolyte. Figure S10. The transmittance changes of the EESD under different potentials. Figure S11. Polyhedral representation of [La^{III}(H₂O)_x(α₂-P₂W₁₇O₆₁)]⁷⁻. Figure S12. The IR spectra of K₇[La(H₂O)_x(α₂-P₂W₁₇O₆₁)]. Figure S13. UV–vis absorption spectra of K₇[La(H₂O)_x(α₂-P₂W₁₇O₆₁)]. Table S1 Comparison of electrochromic and energy storage performance in this work and previous works about POMs-based and inorganic metal oxides electrodes. References [16,21,32,33,51–56] are cited in the Supplementary Materials.

Author Contributions: Conceptualization, X.Q. and Y.Y.; methodology, X.Q. and Y.Y.; validation, L.Z., Z.L. and X.Q.; formal analysis, L.Z., Z.L. and X.Y.; investigation, L.Z., Z.L., J.W. and Z.W.; resources, X.Q. and Y.Y.; data curation, L.Z., H.J. and Z.W.; writing—original draft preparation, L.Z.; writing—review and editing, X.Q.; funding acquisition, X.Q. and Y.Y. All authors have read and agreed to the published version of the manuscript.

Funding: This research was financially supported by the National Natural Science Foundation of China (22071080), the Natural Science Foundation of Jilin Province (YDZJ202101ZYTS175), and the Scientific Research Fund of Education Department of Jilin Province (No. JJKH20210236KJ, JJKH20220234KJ).

Institutional Review Board Statement: Not applicable.

Informed Consent Statement: Not applicable.

Data Availability Statement: Data are contained within the article and Supplementary Materials.

Conflicts of Interest: The authors declare no conflict of interest.

Sample Availability: Samples of the compounds are available from the authors.

References

1. Cai, G.F.; Zhu, R.; Liu, S.Y.; Wang, J.H.; Wei, C.Y.; Griffith, K.J.; Jia, Y.; Lee, P.S. Tunable intracrystal cavity in tungsten bronze-like bimetallic oxides for electrochromic energy storage. *Adv. Energy Mater.* **2022**, *12*, 2103106. [[CrossRef](#)]
2. Wang, S.C.; Jiang, T.Y.; Meng, Y.; Yang, R.G.; Tan, G.; Long, Y. Scalable thermochromic smart windows with passive radiative cooling regulation. *Science* **2021**, *374*, 1501–1504. [[CrossRef](#)] [[PubMed](#)]
3. Liu, Y.; Wang, J.A.; Wang, F.F.; Cheng, Z.C.; Fang, Y.Y.; Chang, Q.; Zhu, J.X.; Wang, L.; Wang, J.P.; Huang, W.; et al. Full-frame and high-contrast smart windows from halide-exchanged perovskites. *Nat. Commun.* **2021**, *12*, 2208178. [[CrossRef](#)] [[PubMed](#)]
4. Xie, Y.; Zhang, H.Y.; Zhang, J.H.; Zhou, T. Ultra-foldable integrated high-performance in-plane micro-supercapacitors from laser-induced selective metallization. *Energy Storage Mater.* **2022**, *51*, 139–148. [[CrossRef](#)]
5. Wang, Y.; Zhao, Y.; Han, Y.Y.; Li, X.Y.; Dai, C.L.; Zhang, X.Q.; Jin, X.T.; Shao, C.X.; Lu, B.; Wang, C.Z.; et al. Fixture-free omnidirectional prestretching fabrication and integration of crumpled in-plane micro-supercapacitors. *Sci. Adv.* **2022**, *8*, eabn8338. [[CrossRef](#)]
6. Shen, M.H.; Ma, H.L. Metal-organic frameworks (MOFs) and their derivative as electrode materials for lithium-ion batteries. *Coord. Chem. Rev.* **2022**, *470*, 214715. [[CrossRef](#)]
7. Wang, C.Y.; Liu, T.; Yang, X.G.; Ge, S.H.; Stanley, N.V.; Rountree, E.S.; Leng, Y.J.; McCarthy, B.D. Fast charging of energy-dense lithium-ion batteries. *Nature* **2022**, *611*, 485–490. [[CrossRef](#)]
8. Yang, W.; Han, Q.K.; Li, W.S.; Wu, M.S.; Yao, J.; Zhao, M.; Lu, X.M. Ti₃C₂T_x MXene as Janus separators for redox-enhanced electrochemical capacitors with reduced self-discharge. *Energy Storage Mater.* **2022**, *52*, 29–39. [[CrossRef](#)]
9. Li, Z.; Wang, X.P.; Zhao, L.Y.; Chi, F.Y.; Gao, C.; Wang, Y.; Yan, M.D.; Zhou, Q.; Zhao, M.M.; Wang, X.Y.; et al. Aqueous hybrid electrochemical capacitors with ultra-high energy density approaching for thousand-volts alternating current line filtering. *Nat. Commun.* **2022**, *13*, 6359. [[CrossRef](#)]
10. Chen, P.; Hu, J.T.; Yu, M.T.; Li, P.C.; Su, R.; Wang, Z.W.; Zhao, L.C.; Li, S.D.; Yang, Y.G.; Zhang, Y.Z.; et al. Refining perovskite heterojunctions for effective light-emitting solar cells. *Adv. Mater.* **2022**, *35*, 2208178. [[CrossRef](#)]

11. Ren, Y.M.; Zhang, D.; Suo, J.J.; Cao, Y.M.; Eickemeyer, F.T.; Vlachopoulos, N.; Zakeeruddin, S.M.; Hagfeldt, A.; Grätzel, M. Hydroxamic acid preadsorption raises efficiency of cosensitized solar cells. *Nature* **2022**, *613*, 60–65. [\[CrossRef\]](#)
12. Zhao, L.L.; Chen, Z.M.; Peng, Y.Q.; Yang, L.L.; Ai, J.T.; Zhou, J.H.; Miao, L. High-performance complementary electrochromic energy storage device based on tungsten trioxide and manganese dioxide films. *Sustain. Mater. Technol.* **2022**, *32*, e00445. [\[CrossRef\]](#)
13. Huang, Q.J.; Wang, J.J.; Gong, H.; Zhang, Q.Q.; Wang, M.Y.; Wang, W.W.; Nshimiyimana, J.P.; Diao, X.G. A rechargeable electrochromic energy storage device enabling effective energy recovery. *J. Mater. Chem. A* **2021**, *9*, 6451–6459. [\[CrossRef\]](#)
14. Khan, F. Attaining remarkable switching speed of nickel oxide-based electrode for electrochromic energy storage devices. *Surf. Interfaces* **2022**, *29*, 101792. [\[CrossRef\]](#)
15. Wang, H.; Yao, C.J.; Nie, H.J.; Yang, L.; Mei, S.L.; Zhang, Q.C. Recent progress in integrated functional electrochromic energy storage devices. *J. Mater. Chem. C* **2020**, *8*, 15507–15525. [\[CrossRef\]](#)
16. Lee, Y.H.; Park, J.Y.; Ahn, K.S.; Sung, Y.E. MnO₂ nanoparticles advancing electrochemical performance of Ni(OH)₂ films for application in electrochromic energy storage devices. *J. Alloys Compd.* **2022**, *923*, 166466.
17. Kim, S.Y.; Jang, Y.J.; Kim, Y.M.; Lee, J.K.; Moon, H.C. Tailoring diffusion dynamics in energy storage ionic conductors for high-performance, multi-Function, single-layer electrochromic supercapacitors. *Adv. Funct. Mater.* **2022**, *32*, 44. [\[CrossRef\]](#)
18. Chiu, C.W.; Huang, C.Y.; Li, J.W.; Li, C.L. Flexible hybrid electronics nanofiber electrodes with excellent stretchability and highly stable electrical conductivity for smart clothing. *ACS Appl. Mater. Interfaces* **2022**, *14*, 42441–42453. [\[CrossRef\]](#)
19. Sun, Y.; Zhao, X.; Zhu, G.Q.; Li, M.; Zhang, X.Q.; Yang, H.; Lin, B.P. Twisted ladder-like donor-acceptor polymers as electrode materials for flexible electrochromic supercapacitors. *Electrochim. Acta* **2020**, *333*, 135495. [\[CrossRef\]](#)
20. Liu, L.; Du, K.; He, Z.B.; Wang, T.; Zhong, X.L.; Ma, T.; Yang, J.M.; He, Y.C.; Dong, G.B.; Wang, S.H.; et al. High-temperature adaptive and robust ultra-thin inorganic all-solid-state smart electrochromic energy storage devices. *Nano Energy* **2019**, *62*, 46–54. [\[CrossRef\]](#)
21. Wang, C.J.; Zhang, X.L.; Liu, S.; Zhang, H.L.; Wang, Q.; Zhang, C.L.; Gao, J.H.; Liang, L.Y.; Cao, H.T. Interfacial charge transfer and zinc ion intercalation and deintercalation dynamics in flexible multicolor electrochromic energy storage devices. *ACS Appl. Energy Mater.* **2021**, *5*, 88–97. [\[CrossRef\]](#)
22. Chen, J.W.; Eh, A.L.S.; Ciou, J.H.; Lee, P.S. Pseudocapacitive and dual-functional electrochromic Zn batteries. *Mater. Today Energy* **2022**, *27*, 101048. [\[CrossRef\]](#)
23. Sun, B.L.; Liu, Z.X.; Li, W.; Huang, H.; Xia, Y.; Gan, Y.P.; Liang, C.; Zhang, W.K.; Zhang, J. A high-performance electrochromic battery based on complementary Prussian white/Li₄Ti₅O₁₂ thin film electrodes. *Sol. Energy Mater. Sol. Cells* **2021**, *231*, 111314. [\[CrossRef\]](#)
24. Deng, C.F.; Zhang, K.; Liu, L.; He, Z.B.; Huang, J.L.; Wang, T.; Liu, Y.S.; He, X.S.; Du, K.; Yi, Y. High-performance all-solid-state electrochromic asymmetric Zn-ion supercapacitors for visualizing energy storage. *J. Mater. Chem. A* **2022**, *11*, 211–217.
25. Zhang, Y.C.; Bai, F.Q.; Xie, Y.F.; Zhu, M.H.; Zhao, L.; An, D.Q.; Xue, D.M.; Berda, E.B.; Wang, C.Y.; Lu, G.Y.; et al. A conjugated polymer with electron-withdrawing cyano group enables for flexible asymmetric electrochromic supercapacitors. *Chem. Eng. J.* **2022**, *450*, 138386. [\[CrossRef\]](#)
26. Horn, M.R.; Singh, A.; Alomari, S.; Goberna-Ferrón, S.; Benages-Vilau, R.; Chodankar, N.; Motta, N.; Ostrikov, K.; MacLeod, J.; Sonar, P.; et al. Polyoxometalates (POMs): From electroactive clusters to energy materials. *Energy Environ. Sci.* **2021**, *14*, 1652–1700. [\[CrossRef\]](#)
27. Win, P.E.P.; Wang, J.X.; Jia, X.Y.; Qi, B.; Chen, W.; He, L.; Song, Y.F. Synergistic effects of polyoxometalate with MoS₂ sheets on multiwalled carbon nanotubes backbone for high-performance supercapacitor. *J. Alloys Compd.* **2020**, *844*, 156194. [\[CrossRef\]](#)
28. Zhang, H.Y.; Ma, Z.Y.; Duan, S.Q.; Liu, Y.; Jiang, X.Y.; Zhou, Q.P.; Chen, M.; Ni, L.B.; Diao, G.W. Dawson-type polyoxometalate modified separator for anchoring/catalyzing polysulfides in high-performance lithium-sulfur batteries. *Electrochim. Acta* **2022**, *428*, 140868. [\[CrossRef\]](#)
29. Wang, G.N.; Chen, T.T.; Gómez-García, C.J.; Zhang, F.; Zhang, M.Y.; Ma, H.Y.; Pang, H.J.; Wang, X.M.; Tan, L.C. A high-capacity negative electrode for asymmetric supercapacitors based on a PMO₁₂ coordination polymer with novel water-assisted proton channels. *Small* **2020**, *16*, 2001626. [\[CrossRef\]](#)
30. Fan, G.; Deng, L.J.; Gu, Y.Z. Replication and capacitive properties of a freestanding phosphomolybdic acid heteropoly blue modified reduced graphite oxide composite. *Sustain. Energy Fuels* **2021**, *5*, 1892–1903. [\[CrossRef\]](#)
31. Zhang, G.U.; Zhang, J.H.; Qiu, T.; Ning, H.L.; Fang, Z.Q.; Zhong, J.Y.; Yang, Y.X.; Yao, R.H.; Luo, D.X.; Peng, J.B. Fabrication of flexible electrochromic film based on amorphous isopolytungstate by low-temperature inkjet-printed process with a solution crystallization kinetic-controlled strategy. *Chem. Eng. J.* **2022**, *427*, 131840. [\[CrossRef\]](#)
32. Liu, S.P.; Zhang, J.; Song, Y.Y.; Feng, S.Y.; Yang, Y.Y.; Qu, X.S. Bifunctional materials containing preyssler-type polyoxometalates and iron phenanthroline stabilized with poly (allylamine hydrochloride) for electrochromic energy storage devices. *Eur. J. Inorg. Chem.* **2022**, *26*, e202200543. [\[CrossRef\]](#)
33. Chu, D.X.; Qu, X.S.; Zhang, S.F.; Zhang, J.; Yang, Y.Y.; An, W.J. Polyoxotungstate-based nanocomposite films with multi-color change and high volumetric capacitance toward electrochromic energy-storage applications. *New J. Chem.* **2021**, *45*, 19977–19985. [\[CrossRef\]](#)

34. Liu, S.P.; Su, X.W.; Chu, D.X.; Ma, C.; Fu, Y.; Qu, X.S.; Lu, J.H.; Guan, H.N. The effect of electrolytes on the electrochromic performance of nickel-substituted tungstophosphate and TiO₂ nanowire composite films. *New J. Chem.* **2021**, *45*, 9375–9381. [[CrossRef](#)]
35. Sullivan, J.L.; Saied, S.O.; Bertoti, I. Effect of ion and neutral sputtering on single crystal TiO₂. *Vacuum* **1991**, *42*, 1203–1208. [[CrossRef](#)]
36. Sullivan, J.L.; Saied, S.O.; Choudhury, T.; Pearce, C.G. A comparison of ion and fast atom beam reduction in TiO₂. *Vacuum* **1988**, *38*, 917–922.
37. Charton, P.; Gengembre, L.; Armand, P. TeO₂–WO₃ glasses: Infrared, XPS and XANES structural characterizations. *J. Solid State Chem.* **2002**, *168*, 175–183. [[CrossRef](#)]
38. Wang, S.M.; Hwang, J.; Kim, E. Polyoxometalates as promising materials for electrochromic devices. *J. Mater. Chem. C* **2019**, *7*, 7828–7850. [[CrossRef](#)]
39. Sun, P.; Liu, H.G.; Ma, X.K.; Zhao, J.H.; Qiu, J.L.; Wang, Y.F.; Zhang, Z.Q. Hierarchical self-supported TiO₂/NC-MoS₂ composite as a stable anode for enhanced lithium-ion batteries. *Int. J. Electrochem. Sci.* **2020**, *15*, 8171–8180. [[CrossRef](#)]
40. Cheng, W.; He, J.F.; Dettelbach, K.E.; Johnson, N.J.J.; Sherbo, R.S.; Berlinguette, C.P. Photodeposited amorphous oxide films for electrochromic windows. *Chem* **2018**, *4*, 821–832. [[CrossRef](#)]
41. Wang, Y.Y.; Jia, X.T.; Zhu, M.H.; Liu, X.C.; Chao, D.M. Oligoaniline-functionalized polysiloxane/prussian blue composite towards bifunctional electrochromic supercapacitors. *New J. Chem.* **2020**, *44*, 8138–8147. [[CrossRef](#)]
42. Liu, S.Q.; Kurth, D.G.; Bredenkötter, B.; Volkmen, D. The structure of self-assembled multilayers with polyoxometalate nanoclusters. *J. Am. Chem. Soc.* **2002**, *124*, 12279–12287. [[CrossRef](#)] [[PubMed](#)]
43. Ilbeygi, H.; Kim, S.; Kim, I.Y.; Joseph, S.; Kim, M.G.; Vinu, A. Super-reductive mesoporous phosphomolybdate with high crystallinity and its excellent performance for Li-ion battery application. *J. Mater. Chem. A* **2022**, *10*, 12132–12140. [[CrossRef](#)]
44. Brown, A.P.; Anson, F.C. Cyclic and differential pulse voltammetric behavior of reactants confined to the electrode surface. *J. Anal. Chem.* **1977**, *49*, 1589–1595. [[CrossRef](#)]
45. Liu, Y.B.; Wang, J.X.; Xiao, X.D.; Cai, X.S.; Sheng, G.Z.; Xu, G. Synthesis of high-performance electrochromic thin films by a low-cost method. *Ceram. Int.* **2021**, *47*, 7837–7844. [[CrossRef](#)]
46. Harmalkar, S.P.; Leparulo, M.A.; Pope, M.T. Mixed-valence chemistry of adjacent vanadium centers in heteropolytungstate anions. I. Synthesis and electronic structures of mono-, di-, and trisubstituted derivatives of α -[P₂W₁₈O₆₂]⁶⁻. *J. Am. Chem. Soc.* **1983**, *105*, 4286–4292. [[CrossRef](#)]
47. Tong, Z.Q.; Liu, S.K.; Li, X.G.; Mai, L.Q.; Zhao, J.P.; Li, Y. Achieving rapid Li-ion insertion kinetics in TiO₂ mesoporous nanotube arrays for bifunctional high-rate energy storage smart window. *Nanoscale* **2018**, *10*, 3254–3261. [[CrossRef](#)]
48. Granadeiro, C.M.; Ferreira, R.A.S.; Soares-Santos, P.C.R.; Carlos, L.D.; Nogueira, H.I.S. Lanthanopolyoxometalates as building blocks for multiwavelength photoluminescent organic–inorganic hybrid materials. *Eur. J. Inorg. Chem.* **2009**, *2009*, 5088–5095. [[CrossRef](#)]
49. Wan, R.; Ma, P.T.; Han, M.D.; Zhang, D.D.; Zhang, C.; Niu, J.Y.; Wang, J.P. Discovery and isolation of the trans-isomers of two 1:2-type lanthanide-containing monolacunary Dawson-type tungstophosphates: [Ln^{III}(α -P₂W₁₇O₆₁)₂]¹⁷⁻ (Ln = La, Ce). *Dalton Trans.* **2017**, *46*, 5398–5405. [[CrossRef](#)]
50. Sadakane, M.; Ostuni, A.; Pope, M.T. Formation of 1:1 and 2:2 complexes of Ce(III) with the heteropolytungstate anion α -[P₂W₁₇O₆₁]¹⁰⁻, and their interaction with proline. The structure of [Ce₂(P₂W₁₇O₆₁)₂(H₂O)₈]¹⁴⁻. *Dalton Trans.* **2002**, 63–67. [[CrossRef](#)]
51. Chen, Y.L.; Wang, Y.; Sun, P.; Yang, P.H.; Du, L.H.; Mai, W.J. Nickel oxide nanoflake-based bifunctional glass electrodes with superior cyclic stability for energy storage and electrochromic applications. *J. Mater. Chem. A* **2015**, *3*, 20614–20618. [[CrossRef](#)]
52. Shi, Y.D.; Sun, M.J.; Zhang, Y.; Cui, J.W.; Wang, Y.; Shu, X.; Qin, Y.Q.; Tan, H.H.; Liu, J.Q.; Wu, Y.C. Structure modulated amorphous/crystalline WO₃ nanoporous arrays with superior electrochromic energy storage performance. *Sol. Energy Mater. Sol. Cells.* **2020**, *212*, 110579. [[CrossRef](#)]
53. Shen, L.X.; Du, L.H.; Tan, S.Z.; Zang, Z.G.; Zhao, C.X.; Mai, W.J. Flexible electrochromic supercapacitor hybrid electrodes based on tungsten oxide films and silver nanowires. *Chem. Commun.* **2016**, *52*, 6296–6299. [[CrossRef](#)]
54. Prasad, A.K.; Park, J.Y.; Kang, S.H.; Ahn, K.S. Electrochemically co-deposited WO₃-V₂O₅ composites for electrochromic energy storage applications. *Electrochim. Acta* **2022**, *422*, 140340. [[CrossRef](#)]
55. Qu, X.S.; Fu, Y.; Ma, C.; Yang, Y.Y.; Shi, D.; Chu, D.X.; Yu, X.Y. Bifunctional electrochromic-energy storage materials with enhanced performance obtained by hybridizing TiO₂ nanowires with POMs. *New J. Chem.* **2020**, *44*, 15475–15482. [[CrossRef](#)]
56. Liu, S.P.; Qu, X.S. Construction of nanocomposite film of Dawson-type polyoxometalate and TiO₂ nanowires for electrochromic applications. *Appl. Surf. Sci.* **2017**, *412*, 189–195. [[CrossRef](#)]

Disclaimer/Publisher’s Note: The statements, opinions and data contained in all publications are solely those of the individual author(s) and contributor(s) and not of MDPI and/or the editor(s). MDPI and/or the editor(s) disclaim responsibility for any injury to people or property resulting from any ideas, methods, instructions or products referred to in the content.